Cartesian Methods for the Shallow Water Equations on a Sphere

John B. Drake Paul N. Swarztrauber
David L. Williamson

April 10, 1997

Abstract

The shallow water equations in a spherical geometry are solved using a 3-dimensional Cartesian method. Spatial discretization of the 2-dimensional, horizontal differential operators is based on the Cartesian form of the spherical harmonics and an icosahedral (spherical) grid. Computational velocities are expressed in Cartesian coordinates so that a problem with a singularity at the pole is avoided. Solution of auxiliary elliptic equations is also not necessary. A comparison is made between the standard form of the Cartesian equations and a rotational form using a standard set of test problems. Error measures and conservation properties of the method are reported for the test problems.

1 Introduction

This report is one of a series of documents developing numerical methods for global climate modeling. The work reported is sponsored by the CHAMMP program of the Department of Energy's Office of Health and Environmental Research. CHAMMP is an acronym for Computer Hardware, Advanced Mathematics and Model Physics. Its goal is the development of advanced climate models with considerably improved throughput, accuracy and realism.

The use of triangular meshes for the solution of PDE's on a spherical domain is attractive for several reasons. Triangles allow nearly uniform meshes while rectangular meshes suffer the problem of varying resolution near the poles. Secondly, triangles require only a simple data structure for use with adaptive mesh techniques or for meshes that resolve irregular features. Adapting a mesh to fit a coastline is an obvious example.

Several early papers investigated the use of icosahedral- triangular meshes [11, 12, 18, 19, 20, 21]. The barotropic vorticity equation and the shallow water equations on the sphere served as the primary equation sets for testing the numerical methods because of their relevance in atmospheric flow models. A review article [22] gives further references of that early work.

More recently an icosahedral method based on the stream function and velocity potential formulation of the shallow water equations with a control volume discretization has been proposed by Masuda [8]. The method was refined and tested on a standard set of cases [23] by Heikes and Randall in [4, 5]. Other icosahedral methods have also been proposed in [2].

Renewed interest in these methods springs from advances in computing and numerical analysis. The introduction of massively parallel computers has prompted the reexamination of many classical algorithms. The granularity of tasks that can be performed in parallel appears to be finer for the finite difference and finite element methods than for spectral transform methods which dominate global atmospheric modeling. This offers the possibility of effective use of many small processors of a parallel computer.

The Cartesian form of the shallow water equations was proposed by Swarztrauber in [23] and further developed in [16]. This alternative formulation avoids the singularity in the velocity at the pole by expressing velocities in a 3-D Cartesian form instead of in spherical coordinates. The introduction of 3-D velocities necessitates a change of the form of the shallow water equations. At first sight this form appears more complicated and probably more expensive computationally. But a closer examination shows the Cartesian formulation to be compact and computationally simple.

The pole problem can also be partially addressed by introducing new scalar variables derived from the velocity. The stream function/velocity potential or the vorticity/divergence function are the usual choices. The resulting system of equations then involves elliptic equations relating the new scalar variables. Since there is no introduction of new scalar variables in the Cartesian formulation, the introduction of elliptic equations is avoided. Thus, the Cartesian method has a significantly lower operation count than those methods requiring the solution of an elliptic equation.

The Cartesian geometry of the sphere and the discretization of the sphere using the points of an icosahedral triangular mesh also lead to a computational economy at the poles. The distances between points of this mesh are nearly uniform and thus there is not a CFL restriction on timestep arising from a longitudinal concentration of points near the pole. There is no need to filter the solution near the poles, a step that can be costly for some methods and that introduces errors on all scales.

The Cartesian formulation was used with the calculation of derivatives using a spectral vector harmonic method in [15]. In this paper we consider the Cartesian formulation with the calculation of derivatives using a stencil of points located on an icosahedral grid. The derivative approximations might be characterized as locally spectral in that they are based on spherical harmonics but only use a local stencil of points like a finite difference method. We show by numerical experiments that the method of approximating differential operators on the icosahedral mesh is accurate and converges as the mesh is refined.

The discretization is then applied to the shallow water equations on a sphere and tested extensively on a set of standard cases for shallow water equation solvers. These tests highlight many of the positive properties of the method as well as expose some of its short comings. We pay particular attention to the conservation properties of the computed solutions. It is found that by changing the formulation of the shallow water equations to a "rotational form", the conservation and energy stability is significantly improved.

2 The Shallow Water Equations on a Sphere

The momentum and mass continuity equations for shallow water flows can be written in advective form

$$\frac{d\mathbf{v}}{dt} = -f\mathbf{k} \times \mathbf{v} - g\nabla h + \mathbf{F}_{\mathbf{v}}, \tag{1}$$

and

$$\frac{dh^*}{dt} = -h^*\nabla \cdot \mathbf{v} + F_h \tag{2}$$

where the substantial derivative is given by

$$\frac{d}{dt}(\ ) \equiv \frac{\partial}{\partial t}(\ ) + \mathbf{v} \cdot \nabla(\ ). \tag{3}$$

The velocity is referred to a rotating Cartesian frame and the components of $\mathbf{v} = (u, v)$ are in the longitudinal and latitudinal directions respectively. The height of the free surface is defined $h = h^* + h_s$ where h^* is the depth of the fluid and. the bottom surface height is given by the time invariant function h_s. External forcing, if present, is included in $\mathbf{F}_{\mathbf{v}} = (F_u, F_v)$ and F_h. This form of the equation is not in conservative form and consequently the numerical methods we develop will not be strictly conservative.

It may be advantageous to evaluate the horizontal (surface) derivatives using a Cartesian form. This form was developed in detail in [16]. By extending the surface vector $\mathbf{v} = (u, v)^T$ to the three-dimensional $\mathbf{v}_s = (w, v, u)^T$ the shallow water equations can be embedded in the system

$$\frac{\partial \mathbf{v}_s}{\partial t} + \mathbf{S}(\mathbf{v}_s)\mathbf{v}_s + \boldsymbol{\alpha} + \boldsymbol{\beta} + \boldsymbol{\gamma} + \boldsymbol{\delta} = 0, \tag{4}$$

where

$$\mathbf{S}(\mathbf{v}_s) = \begin{pmatrix} \frac{\partial w}{\partial r} & \frac{1}{a}(\frac{\partial w}{\partial \theta} - v) & \frac{1}{a\cos\theta}(\frac{\partial w}{\partial \lambda} - u\cos\theta) \\ \frac{\partial v}{\partial r} & \frac{1}{a}(\frac{\partial v}{\partial \theta} + w) & \frac{1}{a\cos\theta}(\frac{\partial v}{\partial \lambda} - u\sin\theta) \\ \frac{\partial u}{\partial r} & \frac{1}{a}\frac{\partial u}{\partial \theta} & \frac{1}{a\cos\theta}(\frac{\partial u}{\partial \lambda} - v\sin\theta + w\cos\theta) \end{pmatrix}, \tag{5}$$

r is the radial coordinate ($r = a$ at the earth's surface) and

$$\boldsymbol{\alpha} = \begin{pmatrix} \frac{u^2+v^2}{a} \\ 0 \\ 0 \end{pmatrix}, \tag{6}$$

$$\boldsymbol{\beta} = \begin{pmatrix} 0 \\ \frac{g}{a}\frac{\partial h}{\partial \theta} \\ \frac{g}{a\cos\theta}\frac{\partial h}{\partial \lambda} \end{pmatrix}, \tag{7}$$

$$\boldsymbol{\gamma} = \begin{pmatrix} 0 \\ -F_v \\ -F_u \end{pmatrix}, \tag{8}$$

and

$$\boldsymbol{\delta} = \begin{pmatrix} 0 \\ fu \\ -fv \end{pmatrix}. \tag{9}$$

If we define $\mathbf{V} = (X, Y, Z)^T$ as the velocity in Cartesian coordinates (x, y, z) then

$$\mathbf{v}_s = \mathbf{Q}\mathbf{V} \tag{10}$$

where

$$\mathbf{Q} = \begin{pmatrix} \cos\theta\cos\lambda & \cos\theta\sin\lambda & \sin\theta \\ -\sin\theta\cos\lambda & -\sin\theta\sin\lambda & \cos\theta \\ -\sin\lambda & \cos\lambda & 0 \end{pmatrix}. \tag{11}$$

Substituting (62) into (57) and multiplying by $\mathbf{Q}^T$ we obtain the Cartesian form

$$\frac{\partial \mathbf{V}}{\partial t} + \mathbf{C}\mathbf{V} + \mathbf{Q}^T(\boldsymbol{\alpha} + \boldsymbol{\beta} + \boldsymbol{\gamma} + \boldsymbol{\delta}) = 0. \tag{12}$$

In this equation

$$\mathbf{C} = \mathbf{Q}^T\mathbf{S}\mathbf{Q} = \begin{pmatrix} \frac{\partial X}{\partial x} & \frac{\partial X}{\partial y} & \frac{\partial X}{\partial z} \\ \frac{\partial Y}{\partial x} & \frac{\partial Y}{\partial y} & \frac{\partial Y}{\partial z} \\ \frac{\partial Z}{\partial x} & \frac{\partial Z}{\partial y} & \frac{\partial Z}{\partial z} \end{pmatrix}, \tag{13}$$

$$\mathbf{Q}^T\boldsymbol{\alpha} = \frac{1}{a^2}\begin{pmatrix} x(X^2+Y^2+Z^2) \\ y(X^2+Y^2+Z^2) \\ z(X^2+Y^2+Z^2) \end{pmatrix}, \tag{14}$$

$$\mathbf{Q}^T\boldsymbol{\delta} = \frac{2\Omega z}{a^2}\begin{pmatrix} 0 & -z & y \\ z & 0 & -x \\ -y & x & 0 \end{pmatrix}\begin{pmatrix} X \\ Y \\ Z \end{pmatrix}, \tag{15}$$

and

$$\mathbf{Q}^T\boldsymbol{\beta} = g\mathbf{P}\nabla_c h \tag{16}$$

where

$$\mathbf{P} = \frac{1}{a^2}\begin{pmatrix} a^2 - x^2 & -xy & -xz \\ -xy & a^2 - y^2 & -yz \\ -xz & -yz & a^2 - z^2 \end{pmatrix}, \tag{17}$$

and

$$\nabla_c h = \left(\frac{\partial h}{\partial x}, \frac{\partial h}{\partial y}, \frac{\partial h}{\partial z}\right)^T. \tag{18}$$

Similarly the continuity equation in Cartesian form is

$$\frac{\partial h^*}{\partial t} + \mathbf{V}^T\mathbf{P}\nabla_c h^* + h^*\nabla_c \cdot \mathbf{V} = F_h. \tag{19}$$

The matrix P projects an arbitrary Cartesian vector onto a plane that is tangent to the sphere at the point (x, y, z).

2.1 Rotational Form of the Momentum Equation

The vorticity ζ is defined in the spherical coordinate system as $\zeta \equiv \mathbf{k} \cdot \nabla \times \mathbf{v}$. Using the vector identity

$$\mathbf{v} \cdot \nabla\mathbf{v} = \nabla(\frac{\mathbf{v} \cdot \mathbf{v}}{2}) + \zeta\mathbf{k} \times \mathbf{v}, \tag{20}$$

the momentum equation can be written

$$\frac{\partial \mathbf{v}}{\partial t} = -(\zeta + f)\mathbf{k} \times \mathbf{v} - \nabla(gh + \frac{\mathbf{v} \cdot \mathbf{v}}{2}) + \mathbf{F}_{\mathbf{v}}. \tag{21}$$

Changing variables to Cartesian velocities the resulting Cartesian equation is

$$\frac{\partial \mathbf{V}}{\partial t} + \mathbf{Q}^T(\boldsymbol{\Lambda} + \boldsymbol{\gamma} + \boldsymbol{\Delta}) = 0. \tag{22}$$

In this equation

$$\mathbf{Q}^T\boldsymbol{\Delta} = \frac{(\zeta + 2\Omega z)}{a^2}\begin{pmatrix} 0 & -z & y \\ z & 0 & -x \\ -y & x & 0 \end{pmatrix}\begin{pmatrix} X \\ Y \\ Z \end{pmatrix}, \tag{23}$$

and

$$\mathbf{Q}^T\boldsymbol{\Lambda} = \mathbf{P}\nabla_c(gh + \frac{\mathbf{V} \cdot \mathbf{V}}{2}). \tag{24}$$

Since the *curl* is invariant under coordinate transformation we have that $\zeta \equiv \mathbf{k} \cdot \nabla_c \times \mathbf{V}$ where $\mathbf{k}$ is the unit vector in the direction normal to the sphere at the point (x, y, z). That is, $\mathbf{k} = \frac{\mathbf{x}}{a}$. (This notation in Cartesian coordinates should not be confused with the standard notation $\mathbf{k}$ for the unit vector in the z-direction.) The Cartesian *curl* is the standard,

$$\nabla_c \times \mathbf{V} = \begin{pmatrix} \frac{\partial Z}{\partial y} - \frac{\partial Y}{\partial z} \\ \frac{\partial X}{\partial z} - \frac{\partial Z}{\partial x} \\ \frac{\partial Y}{\partial x} - \frac{\partial X}{\partial y} \end{pmatrix}. \tag{25}$$

These derivatives are available from the $\mathbf{C}$ matrix described above.

The rotational form of the momentum equation has one excellent property for collocation methods[1]: it is semi-energy conserving. This can be seen by considering the discrete kinetic energy equation obtained by vector multiplication of the momentum equation with the velocity. Ignoring forcing terms and surface orography,

$$\mathbf{V} \cdot \frac{\partial \mathbf{V}}{\partial t} = -\frac{(\zeta + 2\Omega z)}{a^2} \mathbf{V} \cdot \begin{pmatrix} 0 & -z & y \\ z & 0 & -x \\ -y & x & 0 \end{pmatrix} \begin{pmatrix} X \\ Y \\ Z \end{pmatrix} - \mathbf{V} \cdot \mathbf{P} \nabla_c (gh + \frac{\mathbf{V} \cdot \mathbf{V}}{2}). \tag{26}$$

The troublesome advection term is split into two parts, one purely normal to the velocity and the other buried in the gradient as the kinetic energy. The first term vanishes identically when multiplied by the Cartesian velocity because the velocity is tangent to the surface of the sphere.

$$\frac{\partial \frac{\mathbf{V} \cdot \mathbf{V}}{2}}{\partial t} = -\mathbf{V} \cdot \mathbf{P} \nabla_c (gh + \frac{\mathbf{V} \cdot \mathbf{V}}{2}). \tag{27}$$

Defining the total energy by $E = gh + \frac{\mathbf{V} \cdot \mathbf{V}}{2}$ and adding equation (27) to equation (19) the discrete energy equation is

$$\frac{\partial E}{\partial t} = -\mathbf{V} \cdot \mathbf{P} \nabla_c (E) - \mathbf{V} \cdot \mathbf{P} \nabla_c gh - gh \nabla_c \cdot \mathbf{V}. \tag{28}$$

For energy stability, the integral of the discrete energy must be constant,

$$0 = \frac{\partial \overline{E}}{\partial t}, \tag{29}$$

where, by way of notation, the overbar is the integral over the sphere, $\overline{()} = \int_{S^2}()$. Integrating equation (28) yields

$$0 = -\overline{(\mathbf{V} \cdot \mathbf{P} \nabla_c (E))} - \overline{(\mathbf{V} \cdot \mathbf{P} \nabla_c gh + gh \nabla_c \cdot \mathbf{V})}. \tag{30}$$

If the discrete gradient is the negative adjoint of the discrete divergence, the energy equation becomes

$$0 = +\overline{(E \nabla_c \cdot \mathbf{V})} - \overline{(\nabla_c \cdot (gh\mathbf{V}))}. \tag{31}$$

For a divergence free velocity, the first term vanishes, and the second term is the condition of global conservation of mass. So the discrete energy will be conserved if these conditions are met. Using the rotational form in collocation methods improves the nonlinear energy stability of the numerical method and reduces the need for artificial diffusion to enhance stability.

3 Local Cartesian Spectral Approximation

The spherical harmonic functions form a basis for functions defined on the surface of the sphere. They have long been used in climate and weather models as the basis for the spectral method [7] and for the approximation of derivatives on the surface of the sphere [14]. The spherical harmonic, Y_n^m can be defined with the normalized associated Legendre functions $P_n^m(\theta)$ by

$$Y_n^m(\lambda, \theta) = e^{im\lambda} \bar{P}_n^m(\theta). \tag{32}$$

The normalized associated Legendre polynomials can be defined from Rodrigues' formula [13]

$$\bar{P}_n^m(\theta) = (-1)^m \left[\frac{2n+1}{2} \frac{(n-m)!}{(n+m)!} \right]^{1/2} \frac{1}{2^n n!} (\sin\theta)^m \frac{d^{m+n}}{dz^{m+n}} (z^2-1)^n \tag{33}$$

where $z = \cos\theta$ and θ is colatitude. (In this section only θ refers to colatitude while in other sections it refers to latitude.) Equations (32) and (33) are combined to give a formula for the Cartesian representation of the spherical harmonics [17].

$$Y_n^m(x, y, z) = C_n^m (x+iy)^m \frac{d^{m+n}}{dz^{m+n}} (z^2-1)^n, \tag{34}$$

where

$$C_n^m = \frac{(-1)^m}{2^n n!} \left[\frac{2n+1}{2} \frac{(n-m)!}{(n+m)!} \right]^{1/2}. \tag{35}$$

Each spatial field could be approximated in Cartesian coordinates by a series of trivariate polynomials. For example,

$$\phi(x, y, z) = \sum_{m,n} c_n^m Y_n^m(x, y, z), \tag{36}$$

where the c_n^m are coefficients of the trivariate polynomials Y_n^m. To find the c_n^m's in the expression for ϕ, a least squares problem could be solved to fit ϕ data at a set of points on the surface of the sphere with the expansion. Depending on how many points this involves and how many terms are taken in the spectral expansion, this is either a full rank or a rank deficient least squares problem. For example, on an icosahedral grid each grid point has 6 or 7 nearest neighbors. Using a second order interpolant, we have 9 spherical harmonics. This would be a local spectral approximation.

4 Discrete Operator Formulas

Rather than interpolating a field and then differentiating the formula we can alternatively approximate the differential operators directly by requiring that the discrete operators act correctly on the selected basis functions. Given a cluster of points $\{p_l\}$, $l = 0, ..., np-1$ on the surface of the sphere and a tabulation of a function U, $\{U(p_l)\}$ about the point p_0, we wish to determine coefficients c_l such that

$$L(U)(p_0) \approx \sum_{l=0}^{np-1} c_l U(p_l). \tag{37}$$

(The sense of the approximation ($\approx$) must be described.) We require (37) to hold for all spherical harmonics through some number N,

$$L(r^n Y_n^m)(p_0) \cong \sum_{l=0}^{np-1} c_l r^n Y_n^m(p_l). \tag{38}$$

The spherical harmonics Y_n^m are ordered so that with increasing number the degree increases, (see the Appendix for a listing of the harmonics as trivariate polynomials). This system is then solved for the c_l. A different set of c_l are required for each point p_0 and the stencil of points around it. For the shallow water equations, the stencil coefficients are calculated for each of the linear operators $L(U) = \frac{\partial U}{\partial x}, \frac{\partial U}{\partial y}, \frac{\partial U}{\partial z}$, and the Laplacian, ΔU. This approach is general and is applicable to any distribution of points on the sphere.

The sense of the approximation in (37) is as a least squares problem for (38). The problem can be stated in matrix form: find $\mathbf{c}$ which minimizes

$$||\mathbf{Hc} - \mathbf{d}||_2^2 \tag{39}$$

where $\mathbf{H}$ is a $N \times np$ matrix of spherical harmonics evaluated at points of the stencil and $\mathbf{d}$ is the vector of the exact linear operator applied to the harmonics evaluated at the point. The least squares problem can be solved elegantly using the singular value decomposition (SVD) [6]. Let $\mathbf{H} = \mathbf{USV}^T$ be the SVD. The matrix $\mathbf{S}$ =diag$(\sigma_1, \sigma_2, \ldots, \sigma_{np})$ is the matrix of singular values in descending order. The solution to the least squares problem is

$$\mathbf{c} = \mathbf{VS^{-1}U}^T\mathbf{d} \tag{40}$$

The choice of N and np determine the formal accuracy and smoothness of the derivative approximations. In general, we choose np points nearly symmetric about the point p_0. The number of points used in the stencil will determine the efficiency of the method because evaluation of the derivatives requires a combination of values from these neighboring points. For the icosahedral grid,

q	Grid Points	Triangles	h_{min}(km)	h_{max}(km)	h_{ave}(km)	h_{min}/h_{max}
-	12	20	6699.0	6699.0	6699.0	1.0000
0	42	80	3482.0	3938.0	3710.0	0.8843
1	162	320	1613.0	2070.0	1901.0	0.7792
2	642	1280	761.1	1049.0	956.2	0.7255
3	2562	5120	368.4	526.3	478.8	0.7001
4	10242	20480	181.2	263.4	239.5	0.6878

Table 1: Geometric information for icosahedral grids

each point has 5 or 6 immediate neighbors ($np = 7$). (See Figure 1.) If the immediate neighbors of each of these are included in the stencil, then $np = 19$.

A smoothing parameter that can be introduced in the approximation is the truncation level in the SVD solution. The diagonal matrix of singular values, $\mathbf{S}$, can be used to smooth the least squares solution when the system is underdetermined. By truncating the singular values that are smaller than some tolerance, the minimum norm solution for $\mathbf{c}$ is obtained. This truncation gives a solution regardless of the underdetermined or overdetermined nature of the least squares problem. We have found it advantageous to use the same truncation at all points. For $np = 7$, we truncate at six because the primary points of the icosahedron have only five neighbors. The coefficients are unique at these points and of minimum norm at the other points.

4.1 Numerical Results for the Gradient Approximation

The basic icosahedral mesh consists of twenty triangles on 12 grid points. Each of the twelve points of the mesh is connected to five neighboring points. The refinements of this mesh are subdivisions of the twenty base triangles. By placing three points on the edges of each large triangle, one on each side and dividing each triangle into three subtriangles, the $q = 0$ mesh is obtained by projection of the points (and edges) onto the surface of the sphere. Halving this mesh results in the $q = 1$ mesh and again halving gives the $q = 2$ mesh. The number of points in the mesh is given by the formula,

$$GP(q) = 5(2^{2q+3}) + 2 \tag{41}$$

Table 1 gives geometric information about the different icosahedral meshes.

To check the accuracy of the gradient approximations, a test function exhibiting all modes was used,

$$\phi(\lambda, \theta) = a(\exp x + \exp y + \exp z) \tag{42}$$

The errors in the following tables are derived from the Cartesian approximation to the gradient of this function. The exact values of the function at the vertices of the icosahedral mesh are computed and used in the difference formulas to approximate the Cartesian derivatives. The Cartesian gradient is then transformed to spherical coordinates and compared with the exact gradient of ϕ. The error reported is the l^2-error over the points of the icosahedral mesh.

The first question to be answered regards the choice of N and np the number of points in the stencil. Is there an optimal choice for these parameters on a given grid? If $N = 9$, then spherical harmonics of second order are used. If $N = 16$, then third order harmonics are included. For $N = 25$, fourth order harmonics are included. On an icosahedral grid each point is in a cluster of 6 or 7. Adding neighbors of these points with some symmetry leads to either 13 or 19 point clusters. These clusters define the stencil (see Figure 1) of the discrete operator.

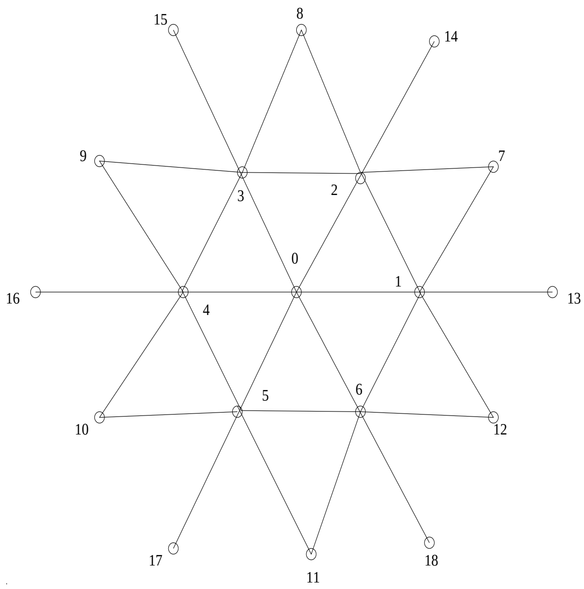

Figure 1: Approximation stencil for a regular point of an icosahedral grid.

Plotting the error in Figure 2 with a log-log scale shows the second order (or greater) convergence of the approximation as the mesh size is decreased. Though the gradient approximations appear to be accurate for higher order spherical harmonics, we will restrict attention in this paper to the quadratic case using $N = 9$ and $np = 7$.

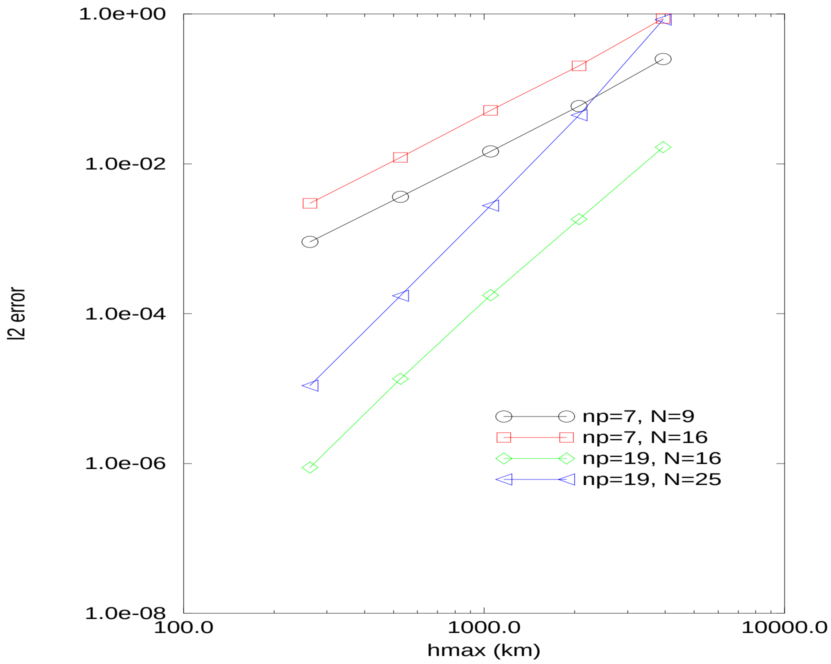

Figure 2: Convergence of the Gradient Approximations.

5 Test Cases

A set of test cases for the shallow water equations on a sphere are detailed in [23]. These cases provide a rigorous test of methods as well as allowing for comparison between methods.

5.1 Advection Test

Test case 1 is a pure advection problem in which a cosine bell is blown around the sphere under a constant velocity field. Figure 3 shows the relative RMS error in the geopotential field as a function of time for a variety of grids. The operators are approximated with quadratic spherical harmonics and use only nearest neighbors. No diffusion was used for this case.

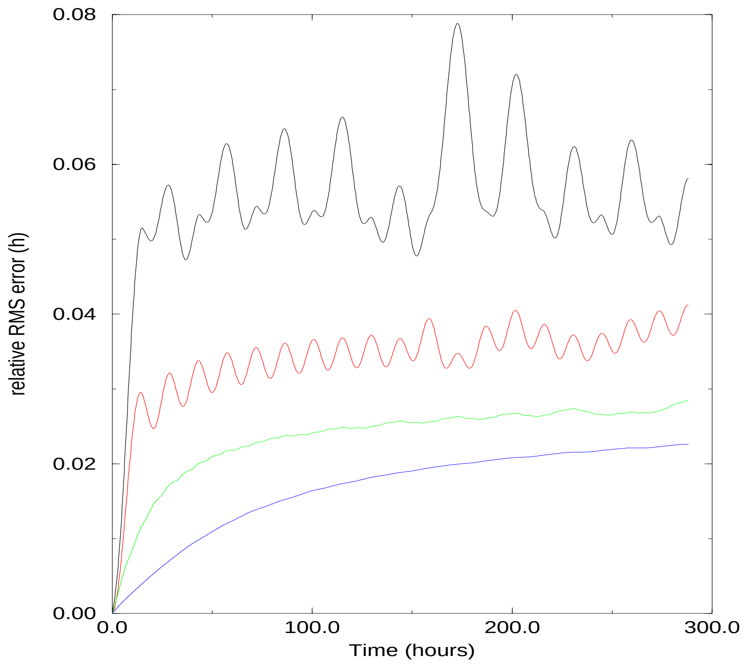

Figure 3: Relative RMS Error in height, Test Case 1, $q = 1, 2, 3, 4$.

5.2 Steady, Zonal Flow Test

Test case 2 is a steady, non-linear zonal flow rotated through an angle $\alpha = \frac{\pi}{4}$. It tests the ability of the code to maintain a steady state solution independent of the grid orientation and gives a good idea of the accuracy of the methods. The velocity and geopotential for this test case are exactly representable with the spherical harmonics of second order. So the local spherical harmonic approximations for the derivative operators are able to capture the steady state solution extremely well. Figure 4 and 5 show the error, as a function of time, in the velocity (using the relative RMS error with the exact steady solution) and the RMS error in the height field, respectively. The $q = 2, 3$ integrations used a time step of 1200 seconds for the 5 day (120 hour) simulations while the $q = 4$ mesh used a 600 second timestep. For the standard formulation, two diffusion terms were added. The momentum equation was modified with a diffusion operator $\epsilon_V \Delta V$ where $\epsilon_V = 8000$. Similarly the height equation was modified with a diffusion coefficient of $\epsilon_h = 20000$. For the rotational formulation, no diffusion was added.

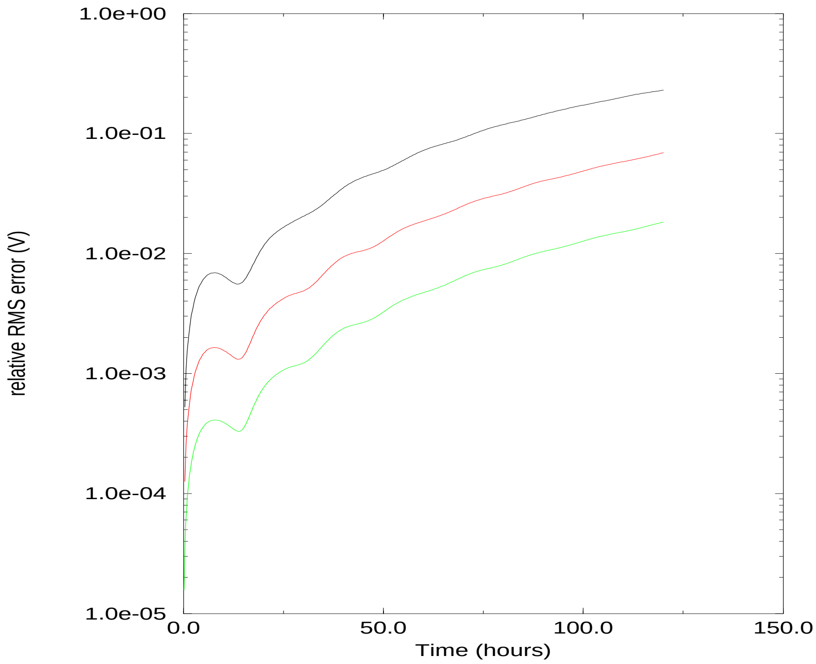

Figure 4: Relative RMS Error in velocity, Test Case 2, $q = 2, 3, 4$. Standard Form

The rotational form gives somewhat better results with no diffusion added. Figure 6 and 7 show the velocity error and the height error for the rotational form of the Cartesian equations also using the serendipitous quadratic approximation on 6 or 7 neighbors. The error growth is much more controlled.

A contor plot of the absolute geopotential error is given in figure 8. The error is measured at 5 days. Clearly evident are the base points of the icosahedral grid where the difference stencil involves 6 rather than 7 points.

The error is held to a small level, but other methods based on latitude-

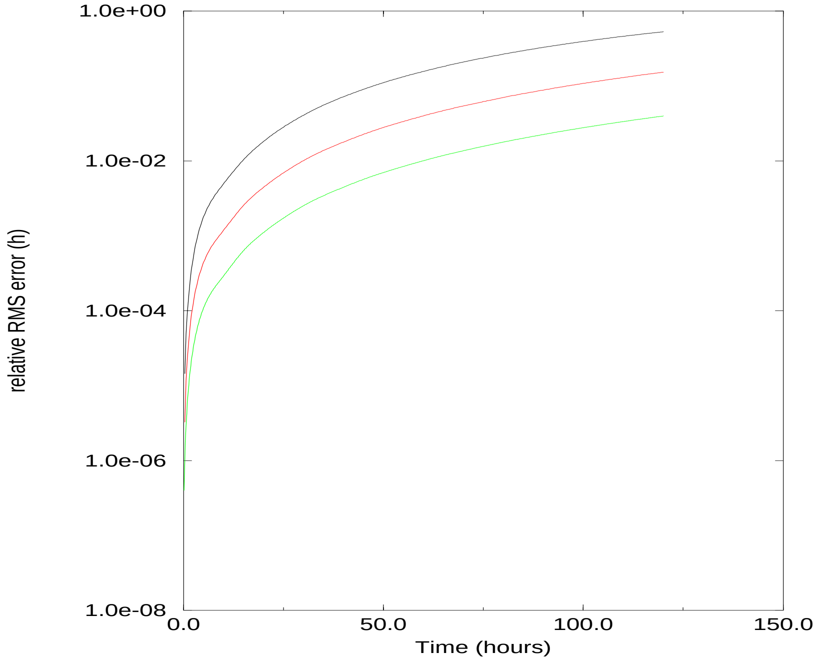

Figure 5: Relative RMS Error in height, Test Case 2, $q = 2, 3, 4$. Standard Form

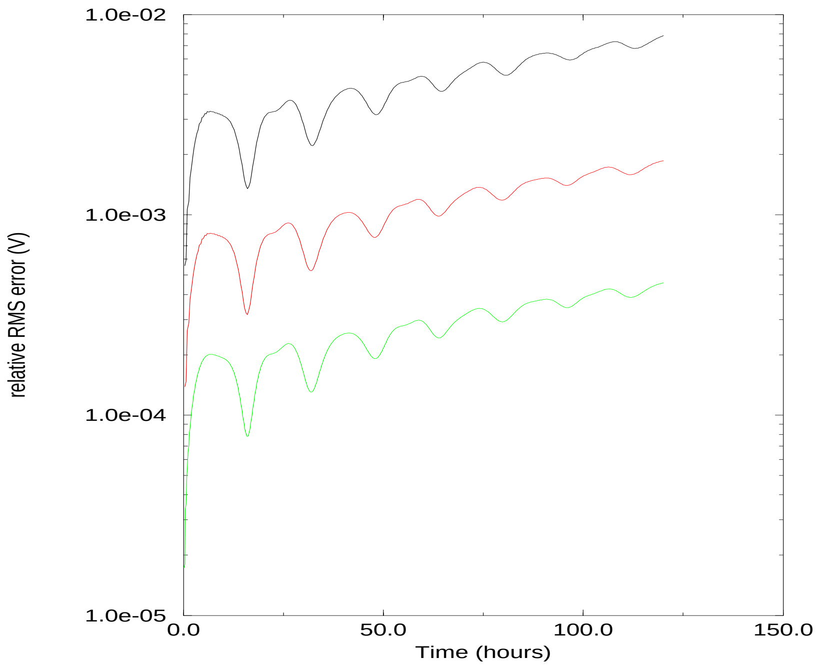

Figure 6: Relative RMS Error in Velocity, Test Case 2, $q = 2, 3, 4$. Rotational Form

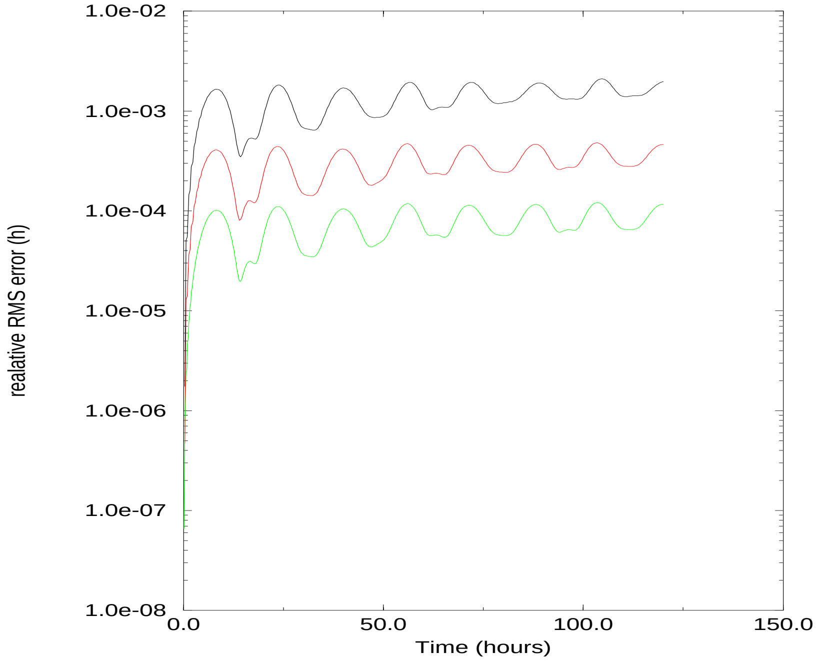

Figure 7: Relative RMS Error in Height, Test Case 2, $q = 2, 3, 4$. Rotational Form

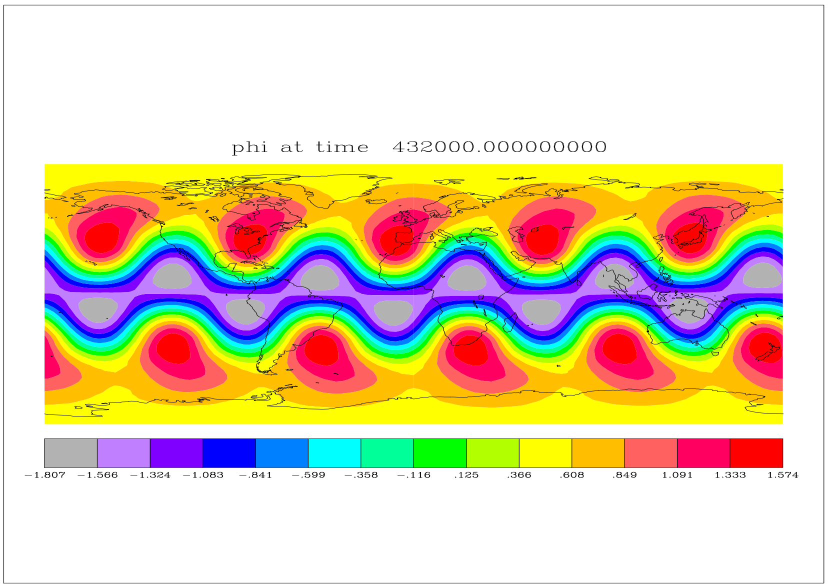

Figure 8: Error in Geopotential at 5 days, Test Case 2, $q = 4$. Rotational Form

longitude grids do not exhibit a systematic error in wave number 5. This raises questions about the influence of the truncation error on the computed solution. What is the expected growth of this error in the nonlinear model due to a perturbation of the initial conditions? To explore this question the computed geopotential from the Cartesian model at 1 day was used as an initial condition in a spectral shallow water equation model, STSWM [3]. The spectral code was run at T42 resolution. After 5 days the STSWM Fourier spectrum at a given latitude is compared to the spectrum of the Cartesian models solution for each day, Figure 9. The Fourier wave amplitude is the square of the modulus of the complex Fourier coefficient of the geopotential. The Fourier coefficients were sampled at the latitude of the T42 spectral model nearest 26.6 degrees, which is the location of one set of icosahedral points and the latitude of highest error in the geopotential.

The solution spectrums to not match but show the same features. The Cartesian solution has a wave 5, 10 and 15 component arising from the icosahedral points. This mode appears to grow over time in the Cartesian model, but no more so than the other modes. The perturbed spectral solution maintains the strong mode 5 components at day 5 with some redistribution of the other modes. The diffusion characteristics of the two methods seem evident. The continued growth of error in the Cartesian model might be attributed to the truncation errors injected in the solution at each timestep. The growth is not a nonlinear mode interaction since the perturbed spectral model shows a preservation of the mode 5 amplitude.

When the Cartesian solution is used as initial conditions in the spectral model, the errors are advected. As these errors, associated with different wave numbers, move around the globe they sometimes cancel to produce smaller errors and other times superimpose to create larger errors. Figure 10 shows the error in the perturbed spectral solution at two different days for the northern hemisphere. The error on day 4 is considerably more dispersed and smaller than the error on day 3 or day 5 indicating a harmonic of the motion. The Cartesian model and the Heikes-Randall model both show 8 peaks of error over the 5 day period. Once an error is present it tends to remain over time, but each model exhibits different numerical diffusion. The Cartesian model shows a much smoother error than the spectral indicating that it is more diffusive than the spectral model. The error profile of the Hiekes-Randall model (see their Figure 9) also shows less diffusion than the Cartesian model. It should be reiterated that no diffusion has been explicitly added to any of these simulations for Case 2.

5.3 Non-Analytic, Steady, Zonal Flow Test

Test case 3 is a steady, non-linear zonal flow rotated through some angle $\alpha = \frac{\pi}{3}$. It is similar to test case 2 but with profiles not exactly representable by the spherical harmonics since they are of compact support. The local spherical

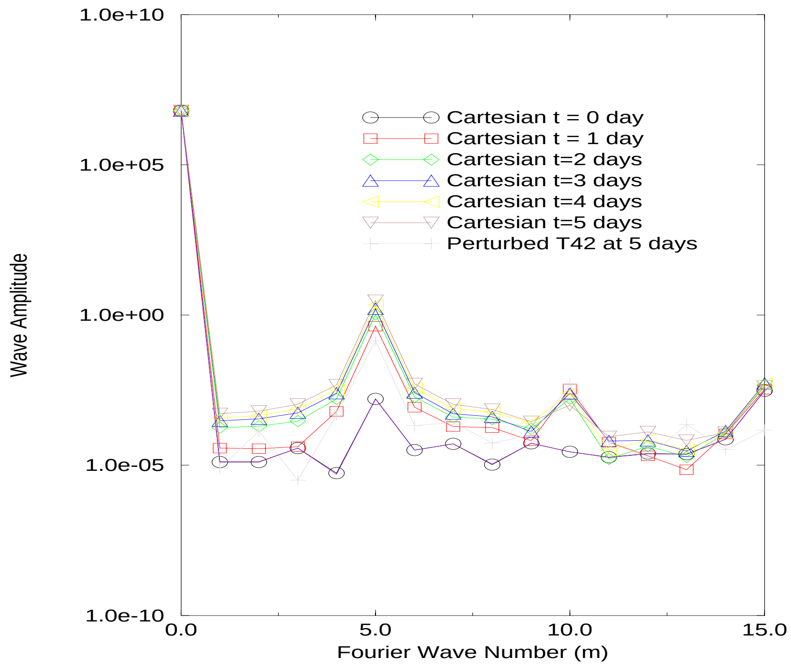

Figure 9: Comparison of geopotential Fourier spectrum for Case 2, $q = 3$. Rotational Form

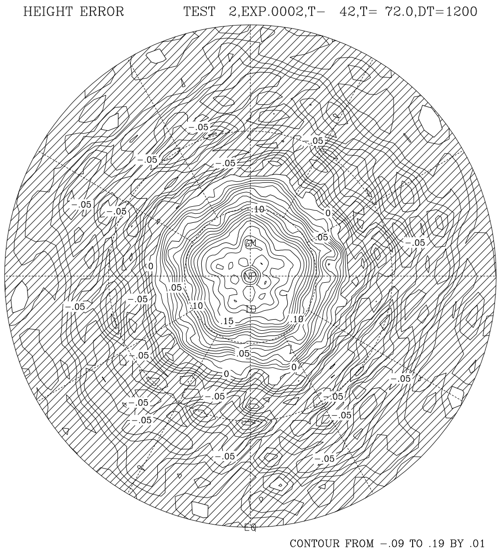

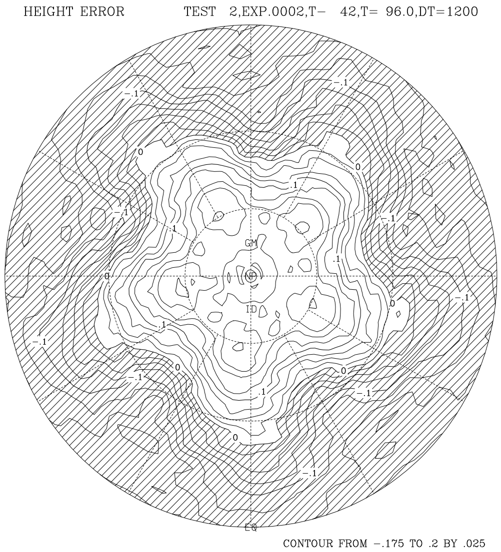

Figure 10: Test Case 2, Perturbed Spectral Geopotential Error (a) at Day 4, (b) at Day 5.

harmonic approximations for the derivative operators are able to capture the steady state solution but not as well as in Test case 2. Figure 11 and 12 show the error, as a function of time, in the velocity (using the relative RMS error with the exact steady solution) and the RMS error in the height field, respectively. Since the model includes no damping the error builds after a time and then grows exponentially. The $q = 2, 3$ integrations used a time step of 1200 seconds for the 5 day (120 hour) simulations while the $q = 4$ mesh used a 600 second timestep. For this case, no explicit diffusion was added to either the momentum or height equations.

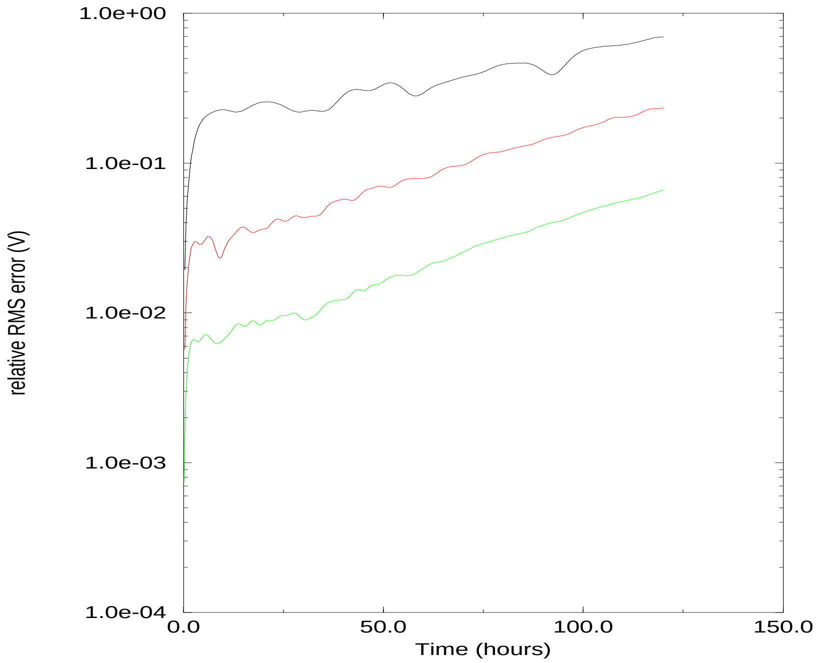

Figure 11: Relative RMS Error in Velocity, Test Case 3, $q = 2, 3, 4$. Standard Form

The rotational form error results for case 3 are given in figures 13 and 14.

A contor plot of the absolute geopotential error is given in figure 15. The error is measured at the 5 days.

5.4 Forced Nonlinear System with a Translating Low

Test case 4 is a time dependent, non-linear forced flow with an exact solution. It tests the performance of the scheme in an unsteady, dynamic simulation. The flow is a translating low pressure center superimposed on a jet stream symmetrical about the equator. The field is similar to a mid-level tropospheric

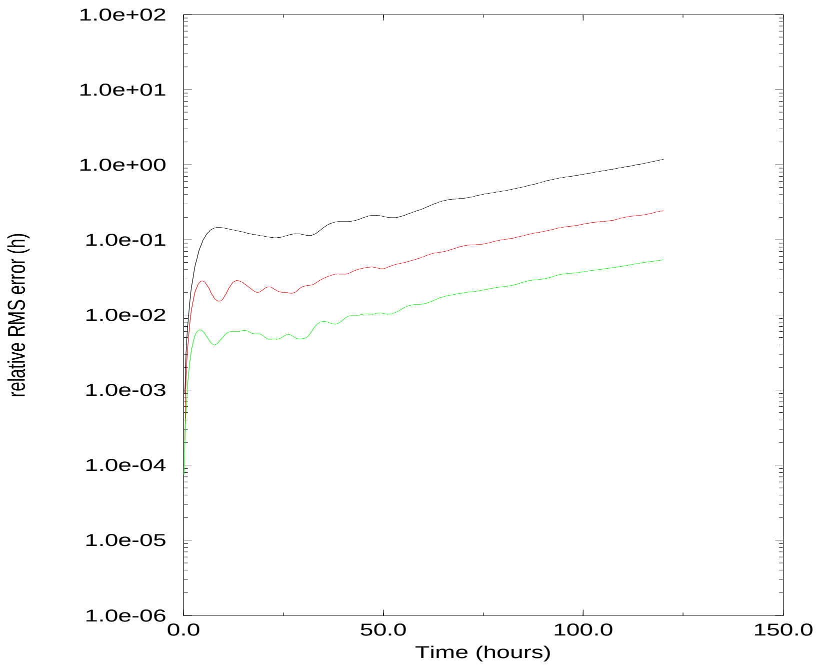

Figure 12: Relative RMS Error in Height, Test Case 3, $q = 2, 3, 4$. Standard Form

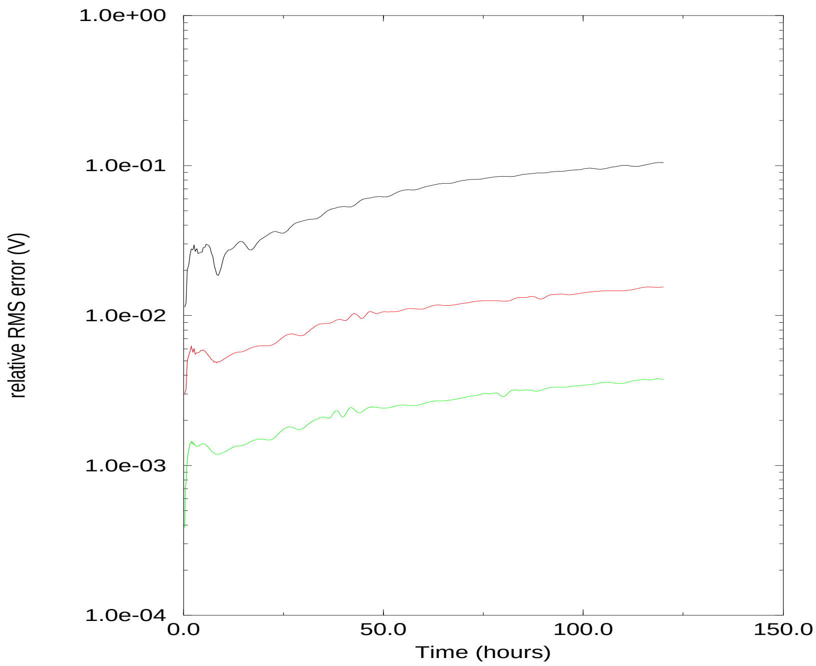

Figure 13: Relative RMS Error in Velocity, Test Case 3, $q = 2, 3, 4$. Rotational Form

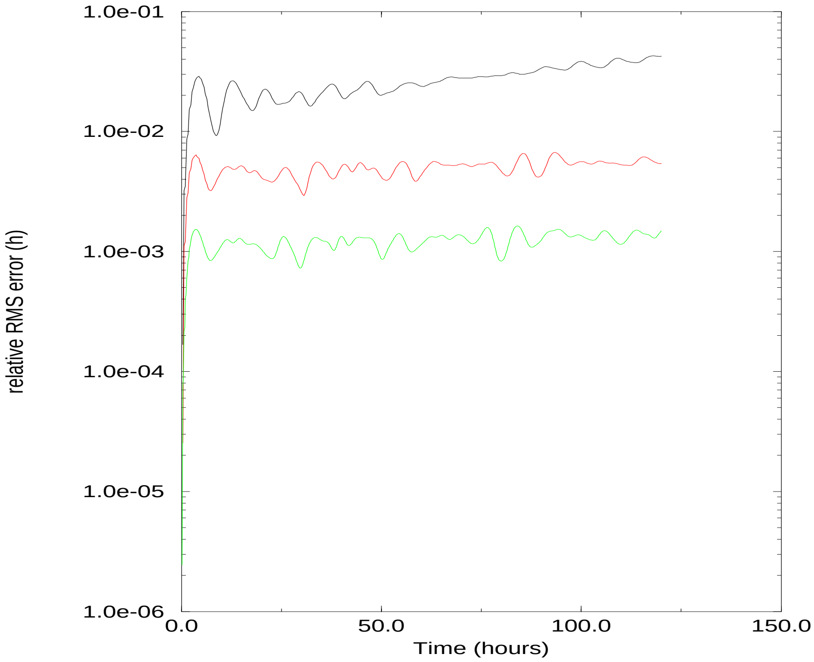

Figure 14: Relative RMS Error in Height, Test Case 3, $q = 2, 3, 4$. Rotational Form

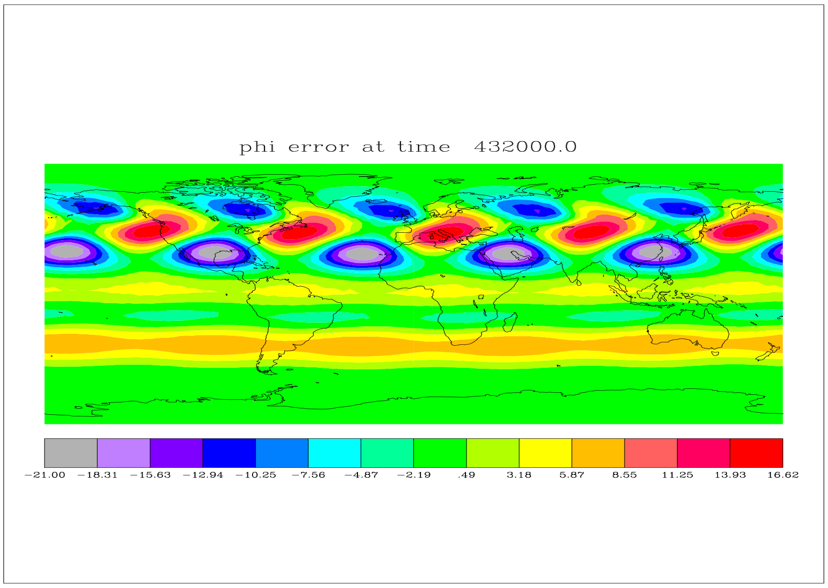

Figure 15: Error in Geopotential at 5 days, Test Case 3, $q = 4$. Rotational Form

flow with a short-wave trough embedded in a westerly jet. As the simulation progress, the low translates eastward maintaining its original shape.

Figure 16 and 17 show the error, as a function of time, in the velocity (using the relative RMS error with the exact solution) and the RMS error in the height field, respectively. The model in rotational form includes no damping. The $q = 2, 3$ integrations used a time step of 1200 seconds for the 5 day (120 hour) simulations while the $q = 4$ mesh used a 600 second timestep. The convergence of the Cartesian method is again exhibited as the mesh is refined.

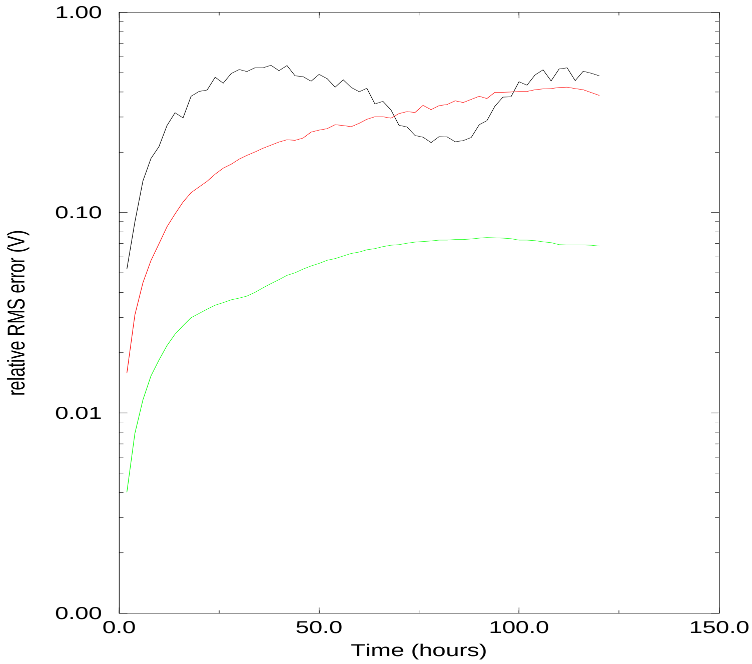

Figure 16: Relative RMS Error in Velocity, Test Case 4, $q = 2, 3, 4$. Rotational Form

5.5 Zonal Flow Over an Isolated Mountain

This test case is the only one with orography. A 5400m mountain is given through the surface height function, h_s. No analytical solution is known for this case so the usefulness of the case is in diagnosing the conservation properties of the numerical scheme. The simulation used a diffusion coefficient of $eps_V = 5.0 \times 10^5$ with a timestep of 600 seconds for the $q = 4$ mesh.

The following normalized integral quantities are presented as a function of time: mass, total energy, potential enstrophy. The vorticity is presented as an integral without normalization in Figure 18. The conservation properties of the

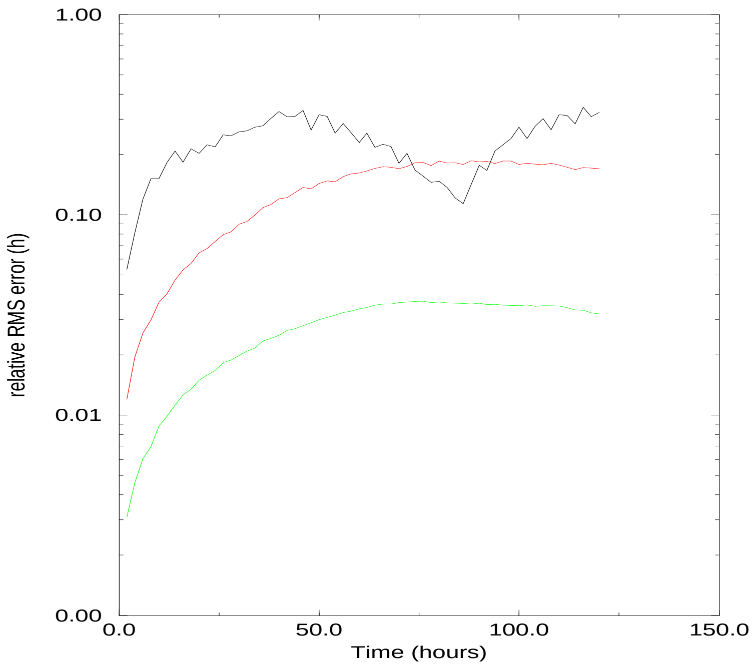

Figure 17: Relative RMS Error in Height, Test Case 4, $q = 2, 3, 4$. Rotational Form

Cartesian method are much better than expected considering that the difference formula used to approximate the conservation of mass are not in flux form and are not guaranteed to preserve the global mass. The excellent conservation of enstrophy and vorticity are also a surprise. As normalized integrals it is not evident from Figure 18 that the integral of enstrophy maintains a value near machine zero ($\approx 10^{-13}$) throughout the simulation.

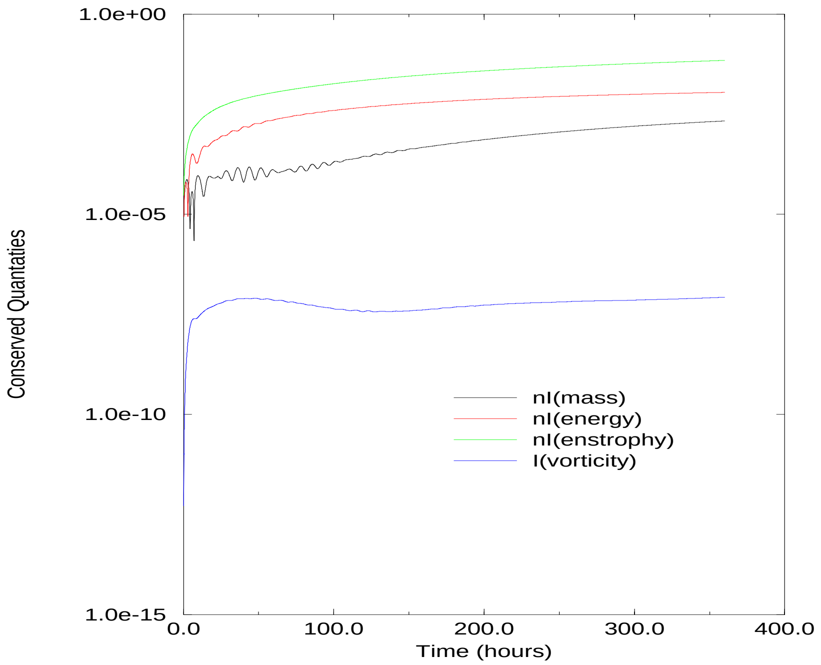

Figure 18: Conserved integral quantities. Test Case 5, $q = 4$. Rotational Form

A contor plot of the geopotential h^* at 15 simulated days is given in Figure 19.

5.6 Rossby-Haurwitz Wave

This classic standard test case [9] does not have an analytic solution for the nonlinear shallow water equations. The initial conditions are zonal wave number 4. The solution at 0, 7, and 14 days continues to show the strong influence of the initial conditions. A diffusion coefficient of $\epsilon_V = 1 \times 10^5$ was used for these calculations. Interestingly, this is close to the value of the diffusion coefficient used by Richardson in [10] and also by Williamson in [21].

The rotational form is semi-conservative of energy. Figures 20 shows the conserved quantities of mass, energy, enstrophy as normalized integrals and the conserved integral of vorticity through the simulation.

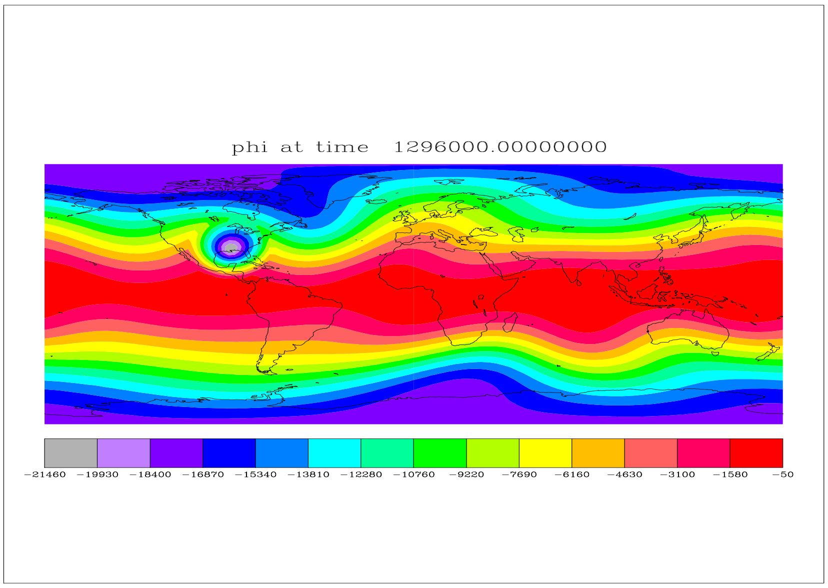

Figure 19: Geopotential at 15 days, Test Case 5, $q = 4$. Rotational Form

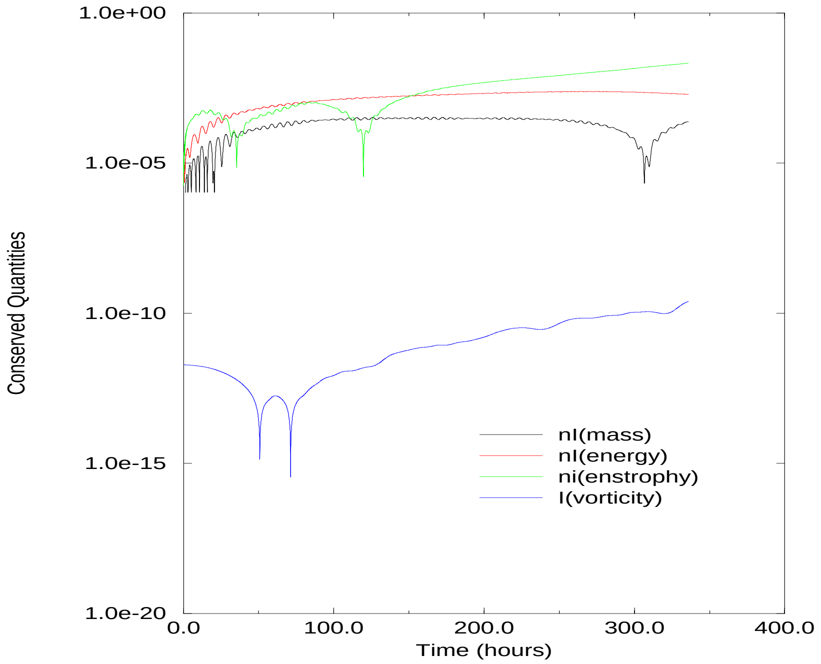

Figure 20: Conserved integral quantities. Test Case 6, $q = 4$. Rotational Form

A contor plot of the geopotential at 14 simulated days is given in Figure 21.

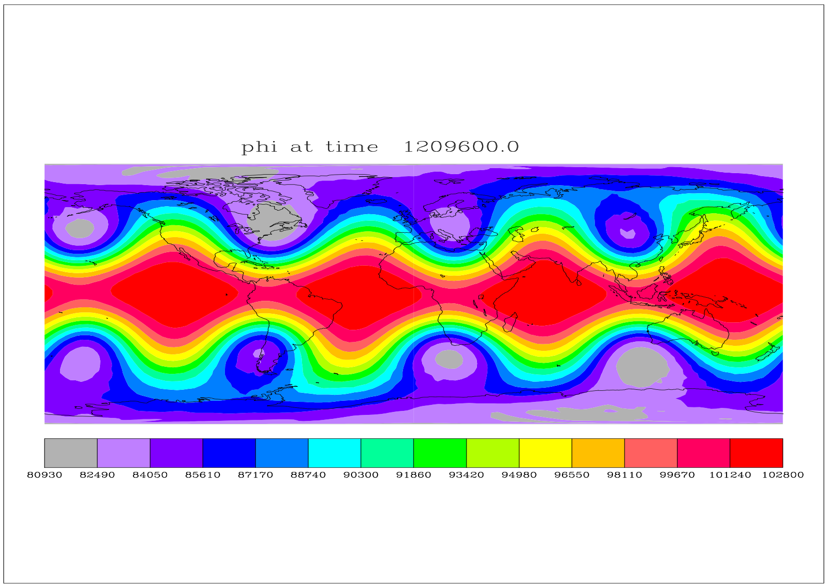

Figure 21: Geopotential at 14 days, Test Case 6, $q = 4$. Rotational Form

Departure of the solution from the initial wave 4 is of interest. To examine the structure of the solution and whether a mode 5 influence is unduly impacting the Cartesian computation, the experiment using the spectral shallow water code, described in test case 2, was repeated. The Cartesian model geopotential output at 1 day was used as an initial condition in a spectral shallow water equation model, STSWM [3]. For reference, the Cartesian solution used for input to the spectral model is plotted in Figure 22. After 5 days the STSWM Fourier spectrum was compared to the spectrum of the Cartesian models solution, at the Gaussian latitude nearest 50 degrees north. Figure 23.

The spectral analysis shows that the growth of low modes in the Cartesian model is similar to the growth in the spectral model. The low modes grow somewhat but are still three orders of magnitude less than mode 4. Modes 1-3 appear stable. Modes 5-7 grow somewhat over the 5 days. In particular, the mode 5 growth is only somewhat larger in the Cartesian model than in the spectral model. This indicates that the solution is exhibiting a (possibly nonlinear) interaction between modes in response to the perturbed initial conditions. The Cartesian method also shows a small compounding of truncation errors due to the icosahedral gird points in mode 5. The distribution of spectral coefficients

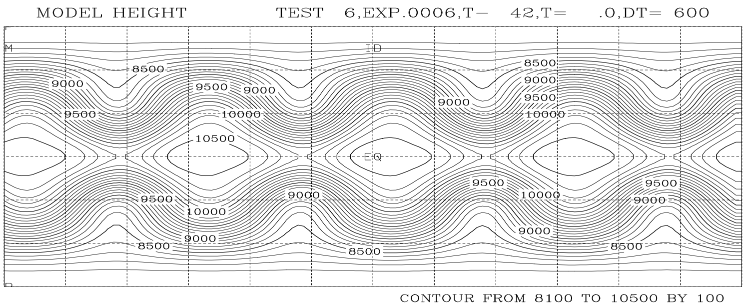

Figure 22: Cartesian Geopotential at Day 1.

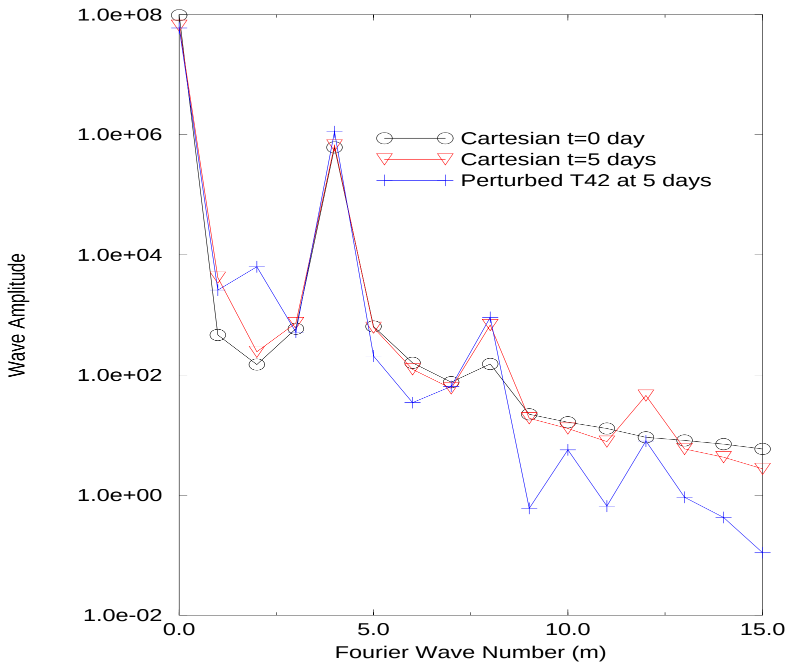

Figure 23: Comparison of geopotential Fourier spectrum for Case 6, $q = 3$. Rotational Form

has more to do with the way energy cascades in the two models. This, in turn, is related to the diffusion of energy inherent in the models.

The solutions of the perturbed spectral model and the Cartesian model differ only slightly by day 5 of the simulation. As seen in Figure 24, the Cartesian exhibits a smoother solution due to the added diffusion. The asymmetry developing by day 14 is not evident but the high latitude departure from wave 4 are manifest. This can be associated with the growth and interaction of the lower wave numbers. The wave 4 interacts with the wave 5 in the perturbation to produce a response in 1 and 9. These waves then interact with the entire spectrum.

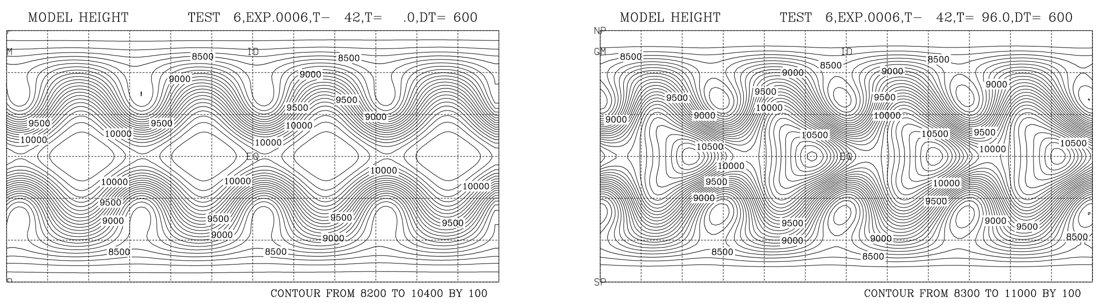

Figure 24: Test Case 6, (a) Cartesian Geopotential at Day 5, (b) Perturbed Spectral Geopotential at Day 5.

5.7 Analyzed 500mb Initial Conditions

The real data initial conditions differ in smoothness from the previous cases exhibiting much finer scale structure and sharper gradients. For non-linear calculations there will be much stronger interaction of modes and more active dispersive phenomena. A diffusion coefficient the same as for test case 6 controls the build up of energy in the fine scales. A timestep of 300 seconds is used on the $q = 4$ mesh with 10242 points.

The first test case using analyzed atmospheric conditions is for 000GMT 21

December 1978. The spectral non-linear normal mode analysis has been used to filter gravity waves from this data. The NCAR netCDF file “REF0077.cdf” was used for initial conditions of both geopotential and velocity at the icosahedral grid points. The strong flow over the north pole has been useful in diagnosing pole problems for several numerical schemes.

Figures 25 shows the conserved quantities of mass, energy, enstrophy as normalized integrals and the conserved integral of vorticity through the simulation.

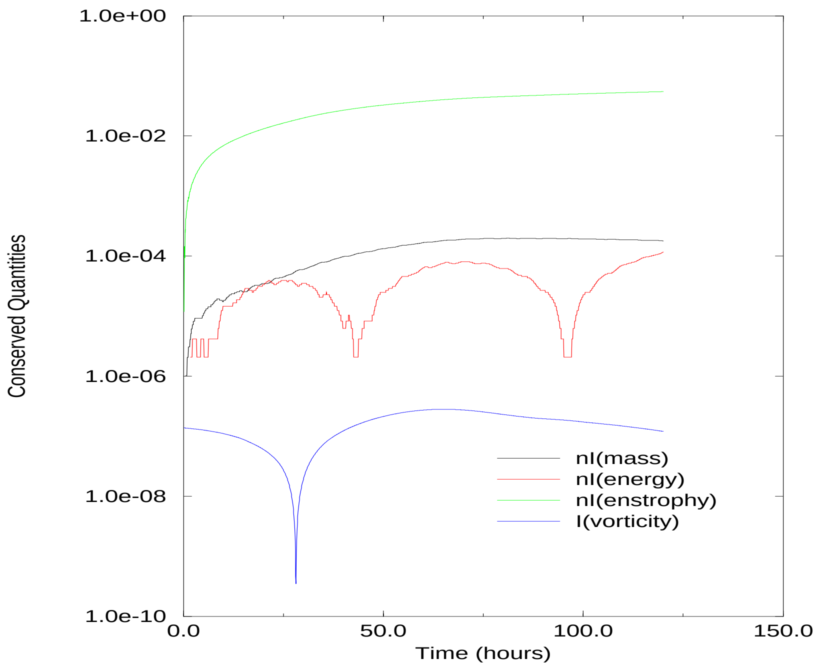

Figure 25: Conserved integral quantities. Test Case 7a, $q = 4$. Rotational Form

Figures 26 and 27 show a comparison of the reference solution with the Cartesian solution at one and five days, respectively.

The second real data case uses the NCAR file “REF0087.cdf”. The flow develops into a typical blocking situation from an initial condition of two cut-off lows. Initial conditions are for 0000 GMT 16 January 1979. Figures 28 and 29 show a comparison of the reference solution with the Cartesian solution at one and five days, respectively.

Figures 30 shows the conserved quantities of mass, energy, enstrophy as normalized integrals and the conserved integral of vorticity through the simulation.

The third real data case has initial conditions from 0000 GMT 9 January 1979 and uses the NCAR file “REF0088.cdf”. Initially it has a strong zonal

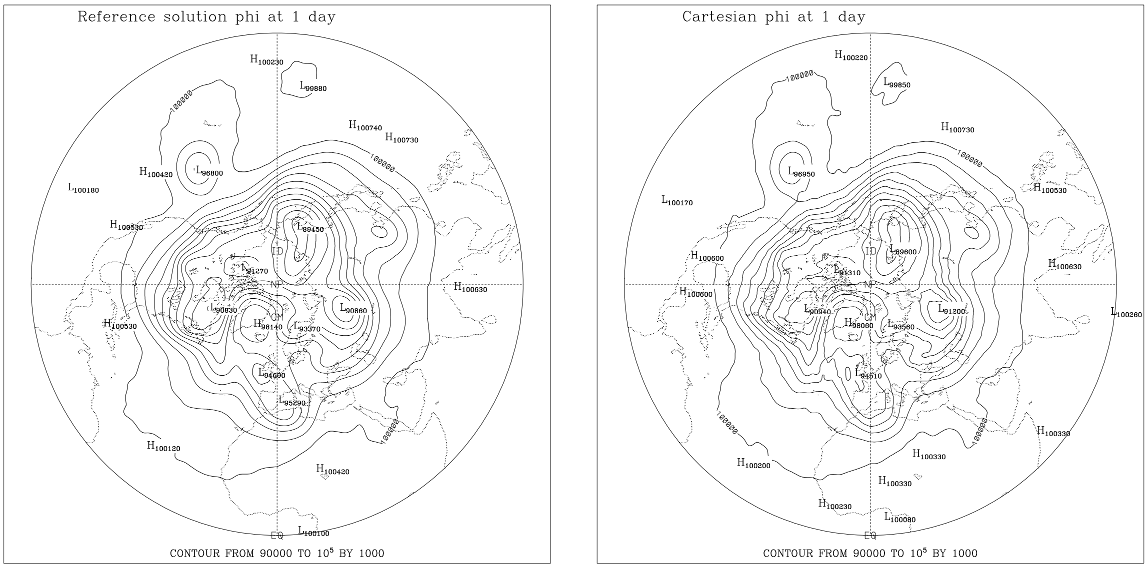

Figure 26: Test Case 7a, (a) Reference Solution at 1 Day, (b) Cartesian Geopotential at 1 Day.

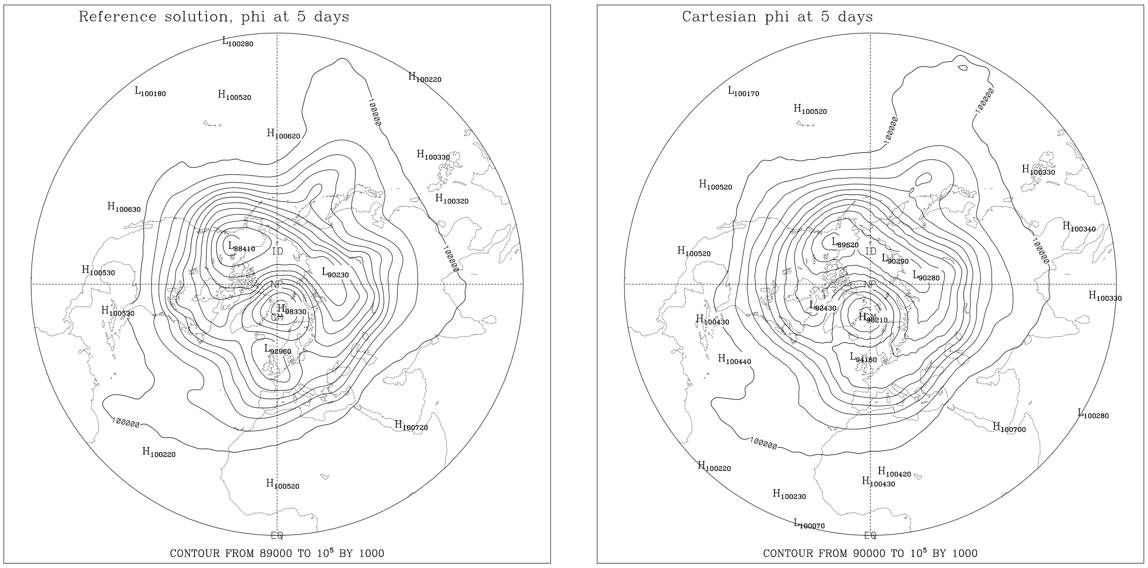

Figure 27: Test Case 7, (a) Reference Solution at 5 Day, (b) Cartesian Geopotential at 5 Day.

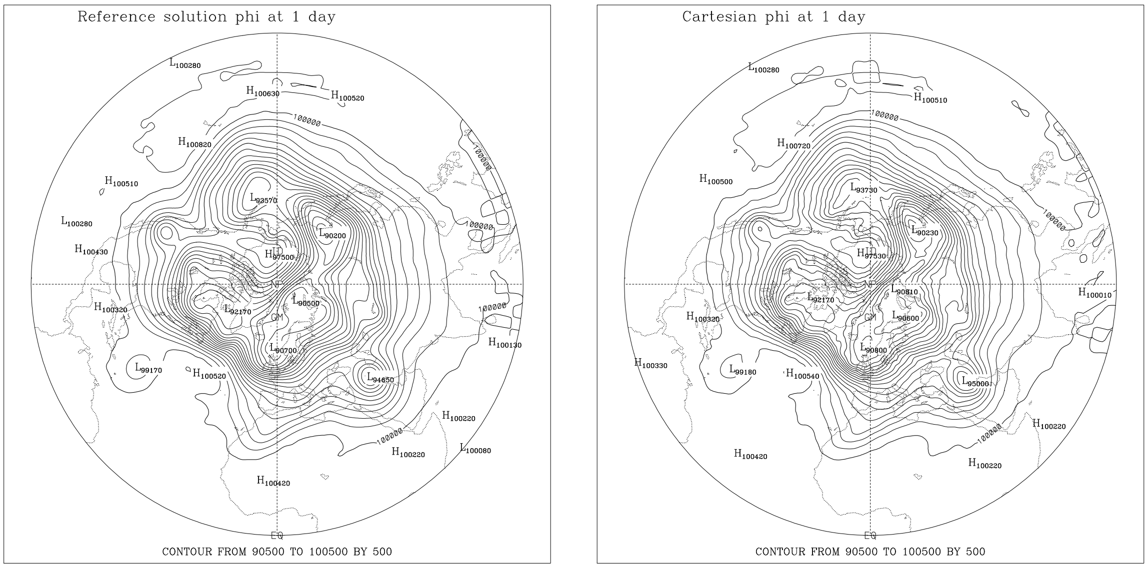

Figure 28: Test Case 7b, (a) Reference Solution at 1 Day, (b) Cartesian Geopotential at 1 Day.

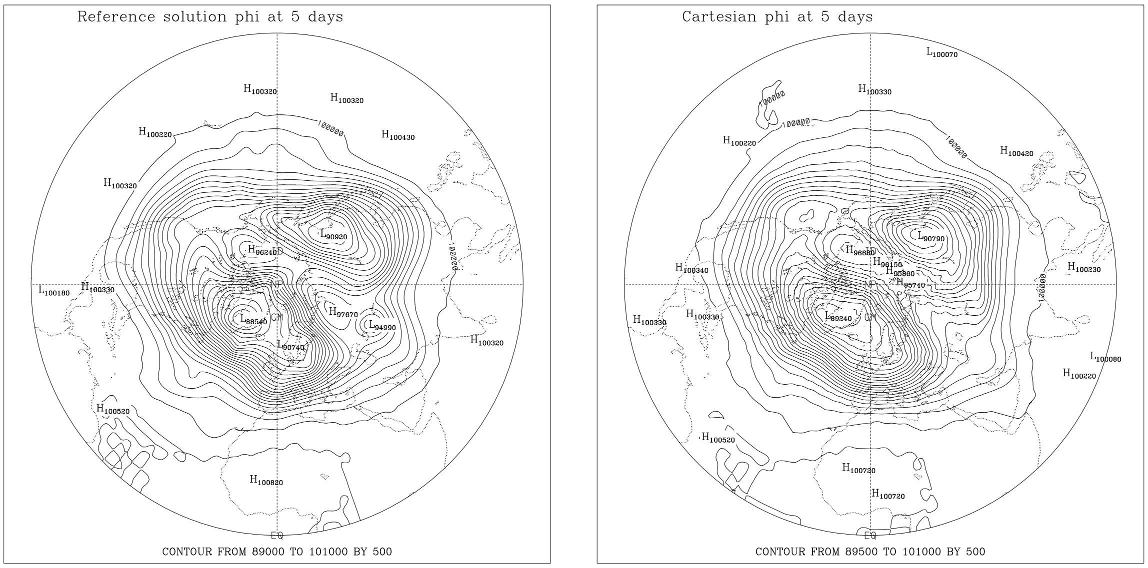

Figure 29: Test Case 7, (a) Reference Solution at 5 Day, (b) Cartesian Geopotential at 5 Day.

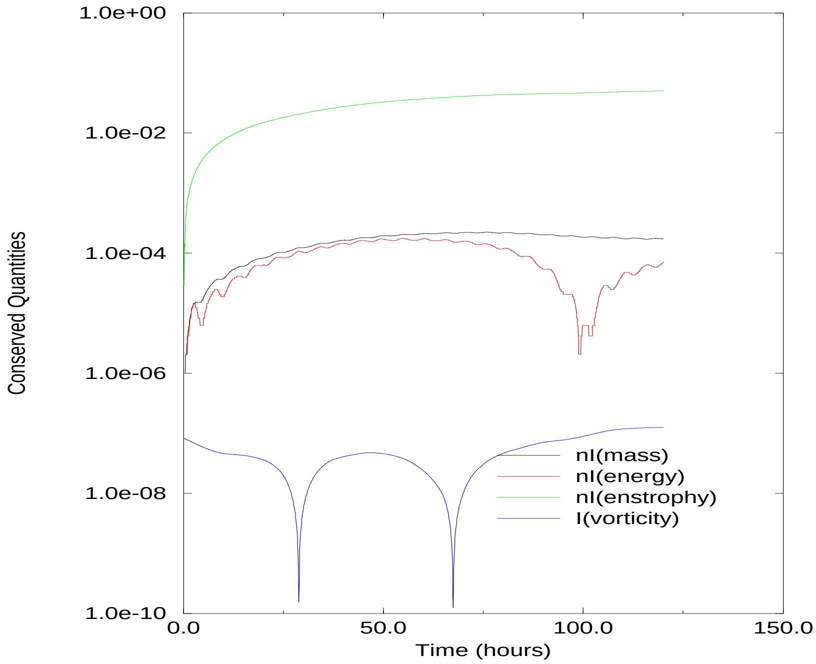

Figure 30: Conserved integral quantities. Test Case 7b, $q = 4$. Rotational Form

flow. Figures 31 and 32 show a comparison of the reference solution with the Cartesian solution at one and five days, respectively.

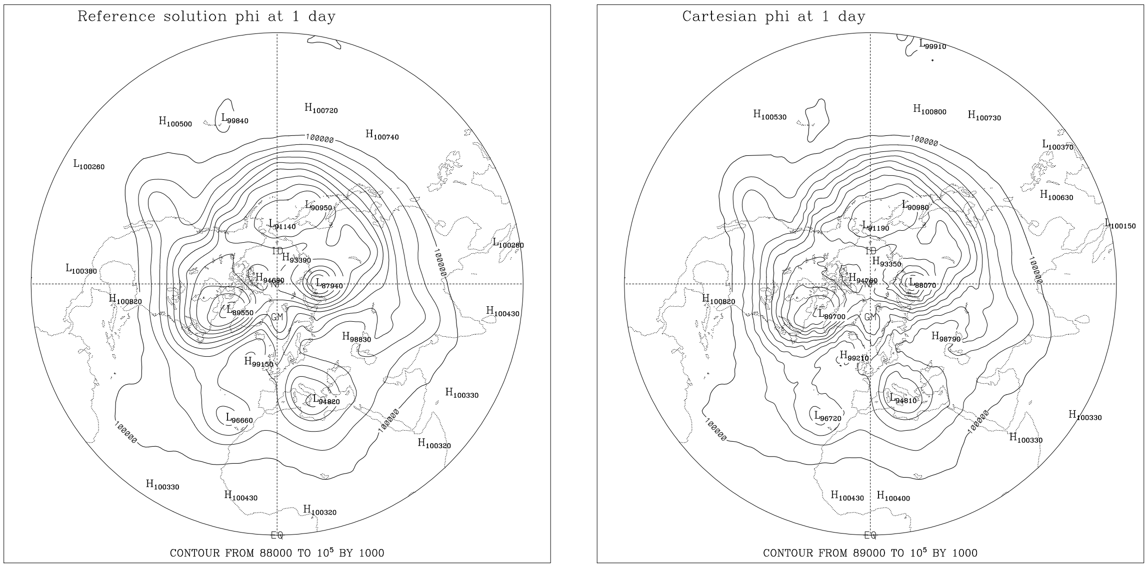

Figure 31: Test Case 7c, (a) Reference Solution at 1 Day, (b) Cartesian Geopotential at 1 Day.

Figures 33 shows the conserved quantities of mass, energy, enstrophy as normalized integrals and the conserved integral of vorticity through the simulation.

5.8 Conclusions

Numerical methods for the shallow water equations on the sphere are faced with three hurdles. First, the accuracy of the geostrophic wind balance. The numerical approximation for the gradient of the geopotential must balance the Coriolis term well. Since the Coriolis term does not involve derivatives the gradient approximation is crucial to achieve a reasonable balance. Second, the pole problem. Since the spherical coordinate representation of the velocity is singular at the poles, derivatives must be approximated with care. The third hurdle is stability. As nonlinear equations, the energy consistency of conversion terms from potential to kinetic energy play a crucial role. In our work, the first hurdle has been passed by adopting a co-located velocity and gradient approximation. The collocation method with accurate approximations for the derivatives gives an excellent balance of the geostrophic wind terms. The Cartesian method is

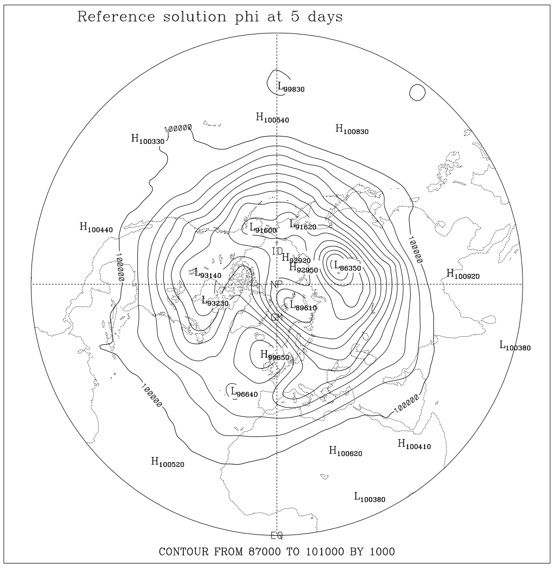

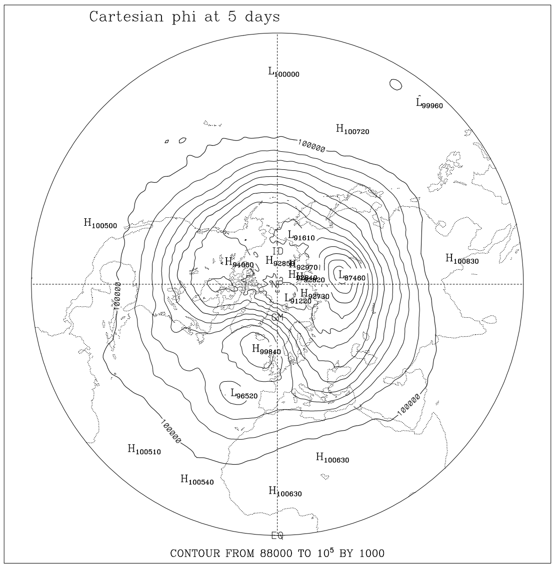

Figure 32: Test Case 7c, (a) Reference Solution at 5 Day, (b) Cartesian Geopotential at 5 Day.

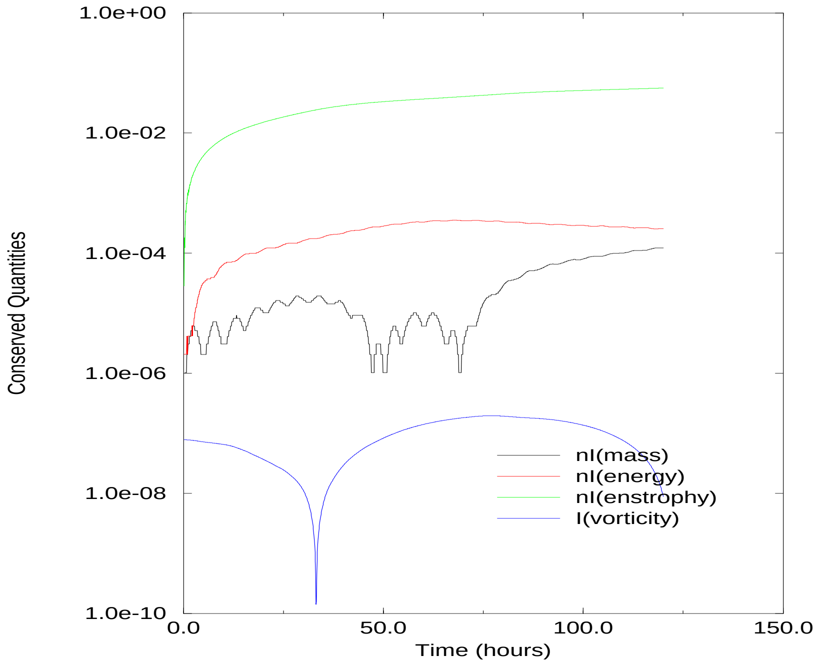

Figure 33: Conserved integral quantities. Test Case 7c, $q = 4$. Rotational Form

free of the pole problem since velocities are continuous at the poles. Finally, the rotational form of the equations in Cartesian form gives reasonably good energy conservation to maintain stability.

The serendipitous use of least squares fitting of the quadratic spherical harmonics to a seven point stencil has given second order convergence for the price of something less. In addition, the Cartesian method does not require the solution of elliptic equations and as a result, has a low operation count.

References

[1] C. Canuto, M.Y. Hussaini, A. Quarteroni, and T.A. Zang. *Spectral Methods in Fluid Dynamcis*. Springer-Verlag, Berlin, 1988.

[2] I-Liang Chern. A control volume method on a icosahedral grid for numerical integration of the shallow-water equations on the sphere - i. Mcs preprint, Argonne National Laboratory, Chicago, IL, 1991.

[3] J.J. Hack and R. Jakob. Description of a global shallow water model based on the spectral transform method. NCAR Technical Note NCAR/TN-343+STR, National Center for Atmospheric Research, Boulder, CO, 1992.

[4] Ross Heikes and David A. Randall. Numerical integration of the shallow-water equations on a twisted icosahedral grid. part i. *Mon. Wea. Rev.*, 123:1862–1880, 1995.

[5] Ross Heikes and David A. Randall. Numerical integration of the shallow-water equations on a twisted icosahedral grid. part ii. *Mon. Wea. Rev.*, 123:1881–1887, 1995.

[6] C.L. Lawson and R.J. Hanson. *Solving Least Squares Problems*. Prentice-Hall, Englewood Cliffs, NJ, 1974.

[7] B. Machenhauer. The spectral method. In *Numerical Methods Used in Atmospheric Models*, volume II of *GARP Pub. Ser. No. 17. JOC*, chapter 3, pages 121–275. World Meteorological Organization, Geneva, Switzerland, 1979.

[8] Y. Masuda and H. Ohnishi. An integration scheme of the primitive equation model with an icosahedral-hexagonal grid system and its application to the shallow water equations. In *Short- and Medium-Range Numerical Weather Prediction*, pages 317–326, 1986.

[9] N. A. Phillips. Numerical integration of the primitive equations on the hemisphere. *Mon. Wea. Rev.*, 87:333–345, 1959.

[10] L.F. Richardson. Atmospheric diffusion shown on a distance neighbour graph. *Proc. Roy. Soc. Ser. A*, 110:709–737, 1928.

[11] R. Sadourny, A. Arakawa, and Y. Mintz. Integration of the nondivergent barotropic vorticity equation with an icosahedral-hexagonal grid for the sphere. *Mon. Wea. Rev.*, 96:351–356, 1968.

[12] R. Sadourny and P. Morel. A finite-difference approximation of the primitive equations for a hexagonal grid on a plane. *Mon. Wea. Rev.*, 97:439–445, 1969.

[13] I. A. Stegun. Legendre functions. In M. Abramowitz and I. A. Stegun, editors, *Handbook of Mathematical Functions*, chapter 8, pages 332–353. Dover Publications, New York, 1972.

[14] P. N. Swarztrauber. The approximation of vector functions and their derivatives on the sphere. *SIAM J. Numer. Anal.*, 18:191–210, 1981.

[15] P.N. Swarztrauber. Spectral transform methods for solving the shallow-water equations on the sphere. *Mon. Wea. Rev.*, 124(4):730–744, 1996.

[16] P.N. Swarztrauber, D.L. Williamson, and J.B. Drake. The cartesian method for solving of PDE's in spherical geometry. *DAO*, to appear.

[17] A.N. Tikhonov and A.A. Samarskii. *Equations of Mathematical Physics.* Dover Publications, New York, 1963.

[18] D. L. Williamson. Integration of the barotropic vorticity equation on a spherical geodesic grid. *Tellus*, 20:642–653, 1968.

[19] D. L. Williamson. Integration of the primitive barotropic model over a spherical geodesic grid. *Mon. Wea. Rev.*, 98:512–520, 1969.

[20] D. L. Williamson. Numerical integration of fluid flow over triangular grids. *Mon. Wea. Rev.*, 97:885–895, 1969.

[21] D. L. Williamson. A comparison of first- and second-order difference approximations over a spherical geodesic grid. *J. Comp. Phys.*, 7:301–309, 1971.

[22] D. L. Williamson. *Numerical Methods Used in Atmospheric Models*, chapter 2, pages 51–120. GARP Pub. Ser. No. 17. JOC, WMO, Geneva, Switzerland, 1979.

[23] D. L. Williamson, J.B. Drake, J.J. Hack, Rudiger Jakob, and P.N. Swarztrauber. A standard test set for numerical approximations to the shallow water equations on the sphere. *J. Comp. Phys.*, pages 211–224, 1992.

A Spherical Harmonic Polynomials

$n = 0$:

$$Y_0^0 = 1$$

$n = 1$:

$$\begin{aligned} rY_1^0 &= z \\ rY_1^1 &= -x - \mathbf{i}\, y \end{aligned}$$

$n = 2$:

$$\begin{aligned} r^2Y_2^0 &= \frac{3}{2}\, z^2 - \frac{1}{2} \\ r^2Y_2^1 &= -3\,(\, x + \mathbf{i}\, y\,)\, z \\ r^2Y_2^2 &= 3\, x^2 + 6\,\mathbf{i}\, x\, y - 3\, y^2 \end{aligned}$$

$n = 3$:

$$\begin{aligned} r^3Y_3^0 &= z^3 + \frac{3}{2}\,(\, z^2 - 1\,)\, z \\ r^3Y_3^1 &= -\frac{1}{48}\,(\, x + \mathbf{i}\, y\,)\,(\, 360\, z^2 - 72\,) \\ r^3Y_3^2 &= 15\,(\, x^2 + 2\,\mathbf{i}\, x\, y - y^2\,)\, z \\ r^3Y_3^3 &= -15\, x^3 + 45\, x\, y^2 - 15\,\mathbf{i}\,(\, 3\, x^2\, y - y^3\,) \end{aligned}$$

$n = 4$:

$$\begin{aligned} r^4Y_4^0 &= z^4 + 3\,(\, z^2 - 1\,)\, z^2 + \frac{3}{8}\,(\, z^2 - 1\,)^2 \\ r^4Y_4^1 &= -\frac{1}{384}\,(\, x + \mathbf{i}\, y\,)\,(\, 3840\, z^3 + 2880\,(\, z^2 - 1\,)\, z\,) \\ r^4Y_4^2 &= \frac{1}{384}\,(\, x^2 + 2\,\mathbf{i}\, x\, y - y^2\,)\,(\, 20160\, z^2 - 2880\,) \\ r^4Y_4^3 &= -105\,(\, x^3 - 3\, x\, y^2 + \mathbf{i}\,(\, 3\, x^2\, y - y^3\,)\,)\, z \\ r^4Y_4^4 &= 105\, x^4 - 630\, x^2\, y^2 + 105\, y^4 + 105\,\mathbf{i}\,(\, 4\, x^3\, y - 4\, x\, y^3\,) \end{aligned}$$

$n = 5$:

$$
\begin{aligned}
r^5 Y_5^0 &= z^5 + 5\,(\,z^2 - 1\,)\,z^3 + \frac{15}{8}\,(\,z^2 - 1\,)^2\,z \\
r^5 Y_5^1 &= -\frac{1}{3840}\,(\,x + \mathbf{i}\,y\,)\,\left(57600\,z^4 + 86400\,(\,z^2 - 1\,)\,z^2 + 7200\,(\,z^2 - 1\,)^2\right) \\
r^5 Y_5^2 &= \frac{1}{3840}\,(\,x^2 + 2\,\mathbf{i}\,x\,y - y^2\,)\,(\,403200\,z^3 + 201600\,(\,z^2 - 1\,)\,z\,) \\
r^5 Y_5^3 &= -\frac{1}{3840}\,(\,x^3 - 3\,x\,y^2 + \mathbf{i}\,(\,3\,x^2\,y - y^3\,)\,)\,(\,1814400\,z^2 - 201600\,) \\
r^5 Y_5^4 &= 945\,(\,x^4 - 6\,x^2\,y^2 + y^4 + I\,(\,4\,x^3\,y - 4\,x\,y^3\,)\,)\,z \\
r^5 Y_5^5 &= -945\,x^5 + 9450\,x^3\,y^2 - 4725\,x\,y^4 - 945\,\mathbf{i}\,(\,5\,x^4\,y - 10\,x^2\,y^3 + y^5\,)
\end{aligned}
$$

$n = 6$:

$$
\begin{aligned}
r^6 Y_6^0 &= z^6 + \frac{15}{2}\,(\,z^2 - 1\,)\,z^4 + \frac{45}{8}\,(\,z^2 - 1\,)^2\,z^2 + \frac{5}{16}\,(\,z^2 - 1\,)^3 \\
r^6 Y_6^1 &= -\frac{1}{46080}(\,x + \mathbf{i}\,y\,)\,\left(967680\,z^5 + 2419200\,(\,z^2 - 1\,)\,z^3 + 604800\,(\,z^2 - 1\,)^2\,z\right) \\
r^6 Y_6^2 &= \frac{1}{46080}(\,x^2 + 2\,\mathbf{i}\,x\,y - y^2\,) \\
&\quad \left(9676800\,z^4 + 9676800\,(\,z^2 - 1\,)\,z^2 + 604800\,(\,z^2 - 1\,)^2\right) \\
r^6 Y_6^3 &= -\frac{1}{46080} \\
&\quad (\,x^3 - 3\,x\,y^2 + \mathbf{i}\,(\,3\,x^2\,y - y^3\,)\,)\,(\,58060800\,z^3 + 21772800\,(\,z^2 - 1\,)\,z\,) \\
r^6 Y_6^4 &= \frac{1}{46080} \\
&\quad (\,x^4 - 6\,x^2\,y^2 + y^4 + \mathbf{i}\,(\,4\,x^3\,y - 4\,x\,y^3\,)\,)\,(\,239500800\,z^2 - 21772800\,) \\
r^6 Y_6^5 &= -10395\,(\,x^5 - 10\,x^3\,y^2 + 5\,x\,y^4 + \mathbf{i}\,(\,5\,x^4\,y - 10\,x^2\,y^3 + y^5\,)\,)\,z \\
r^6 Y_6^6 &= 10395\,x^6 - 155925\,x^4\,y^2 + 155925\,x^2\,y^4 - 10395\,y^6 \\
&\quad + 10395\,\mathbf{i}\,(\,6\,x^5\,y - 20\,x^3\,y^3 + 6\,x\,y^5\,)
\end{aligned}
$$